Biosensors and Bioelectronics 142 (2019) 111580

Contents lists available at ScienceDirect

Biosensors and Bioelectronics

journal homepage: www.elsevier.com/locate/bios

Electrochemical immunosensor based on MoS_2 NFs/Au@AgPt YNCs as signal amplification label for sensitive detection of CEA

Enhui Ma, Ping Wang*, Qingshan Yang, Haoxuan Yu, Fubin Pei, Yueyun Li, Qing Liu, Yunhui Dong**

School of Chemistry and Chemical Engineering, Shandong University of Technology, 255049, Zibo, PR China

ARTICLE INFO

Keywords:
Sandwich-type electrochemical immunosensor
CEA
Au TNPs
MoS_2 NFs/Au@AgPt YNCs

ABSTRACT

Medically, the dynamic change of carcinoembryonic antigen (CEA) concentration has been an important indicator for monitoring and diagnosing tumors. The sensitive and early detection of CEA plays a momentous role in the prevention and diagnosis of cancer and the evaluation of treatment efficiency. In this work, a sensitive sandwich-type electrochemical immunosensor was fabricated for the quantitative detection of CEA. The trimetallic yolk-shell Au@AgPt nanocubes (Au@AgPt YNCs) loaded on amino-functionalized MoS_2 nanoflowers (MoS_2 NFs/Au@AgPt YNCs) were used as the labels to conjugate with secondary antibodies. The Au@AgPt YNCs with internal space and permeable shell improved catalytic active surface area. The nanosheet-based MoS_2 NFs with good catalytic activity were used as carriers to load Au@AgPt YNCs effectively. Due to the biphasic synergistic catalysis, MoS_2 NFs/Au@AgPt YNCs catalyzed the reduction of H_2O_2 effectually to amplify the current signal. Besides, Au triangular nanoprisms (Au TNPs) were used as substrate material to increase the effective contact areas with the surface of electrode and accelerate the interface electron transfer. Under the optimal conditions, a broad linear range from 10 fg mL^{-1} to 100 ng mL^{-1} with low detection limit of 3.09 fg mL^{-1} (S/N = 3) for detecting CEA was obtained. Moreover, the detection results of the human serum samples were satisfactory, indicating the fabricated immunosensor had potential application values in the early clinical analysis.

1. Introduction

Carcinoembryonic antigen (CEA), as a tumor-associated glycoprotein, has been identified as a broad-spectrum tumor marker to indicate the presence and progression of multiple tumors (Limbut et al., 2006; Liu, 2008). Generally, the level of CEA above 5.0 ng mL^{-1} will trigger an examination to look for possible diseases, because their elevated concentrations in human serum pose a risk of cancer (Litvak et al., 2014; Smolej and Benesova, 2010). Therefore, the sensitive and accurate detection of CEA is essential for early clinical diagnosis of cancer.

In recent years, the different bioanalytical methods have been applied in the detection of multiple analytes, such as chemiluminescent immunoassay (Lohani et al., 2012), the enzyme-linked immunosorbent assay (Dixit et al., 2010), the fluorescent immunoassay (Pan et al., 2017), the electrochemical biosensors (Baghayeri et al., 2014, 2018a) and the radioimmunoassay (Venge et al., 2010). Among these methods, the electrochemical biosensors have attracted extensive attention due to its good selectivity, rapid response, and low manufacturing costs (Baghayeri et al., 2018b; Baghayeri and Veisi, 2015). The sandwich-type electrochemical immunosensor is based on highly specific interaction between a couple of match antibodies and antigen. This method primarily utilizes the nanomaterials as labels of secondary antibodies (Ab_2) for signal amplification. Hence, it is crucial to seek the high-performances nanomaterials to improve the sensitivity of sandwich-type electrochemical immunosensor in the detection of CEA.

In this study, the trimetallic yolk-shell Au@AgPt nanocubes (Au@AgPt YNCs) loaded on amino-functionalized MoS_2 nanoflowers (MoS_2 NFs/Au@AgPt YNCs) were used as labels of Ab_2 to improve the sensitivity of the immunosensor. Yolk-shell nanomaterials, the new class of core-shell nanostructures, have attracted much attention in nanoreactors, drug delivery and catalysis (Liu et al., 2012a; Wang et al., 2013). Compared with core-shell nanomaterials, yolk-shell nanomaterials with the distinctive core-void-shell structure possess larger void space, higher surface area and lower density (Choi et al., 2013; Guo et al., 2015). Herein, the Au@AgPt YNCs contained internal space between the Au core and external AgPt alloy shell. The external AgPt alloy

* Corresponding author.
** Corresponding author.
E-mail addresses: wangping876@163.com (P. Wang), dyh651118@126.com (Y. Dong).

https://doi.org/10.1016/j.bios.2019.111580
Received 11 June 2019; Received in revised form 27 July 2019; Accepted 8 August 2019
Available online 10 August 2019
0956-5663/

shell could allow molecules to penetrate and exude from the inside of shell to improve the catalytic activity of the overall structure (Teng et al., 2014). Meanwhile, the presence of a cavity in the Au@AgPt YNCs interior provided a homogenous environment to retain specific molecules for long enough to occur synergistic catalysis between the Au, Ag and Pt nanoparticles (Hong et al., 2013; Londono-Calderon et al., 2016). The internal space and permeable shell offered high surface area and more catalytic active sites, thus Au@AgPt YNCs exhibited excellent catalytic activity for the reduction of H_2O_2. In order to load more active probes and active domains for biomolecular binding, the three-dimensional nanosheet-based MoS_2 nanoflowers (MoS_2 NFs) were synthesized as large carriers to load Au@AgPt YNCs. Compared with two-dimensional MoS_2 nanosheets, the unique hierarchical structure of MoS_2 NFs offered more exposed edges and catalytic active sites, thereby improving the catalytic activity for the reduction of H_2O_2 (Hu et al., 2014). In addition, the as-prepared MoS_2 NFs/Au@AgPt YNCs nanocomposites improved the poor biocompatibility and conductivity of MoS_2 NFs due to the interaction between MoS_2 NFs and Au@AgPt YNCs (Xie et al., 2013). On the one hand, MoS_2 NFs/Au@AgPt YNCs were able to act as carriers to immobilize Ab_2 by the stable metal-N covalent bond between Au@AgPt YNCs and $–NH_2$ on Ab_2 (Xu et al., 2018; Zhou et al., 2014); on the other hand, it could catalyze the reduction of H_2O_2 to amplify the current signal effectively.

The Au nanomaterials are wildly used for the modification of electrode surface in the fabrication of biosensors (Gupta et al., 2013; Yola et al., 2015). The nano-sized Au nanoparticles can enhance the electrode conductivity and accelerate the interface electron transfer (Yola and Atar, 2014; Yola et al., 2013). Herein, the Au triangular nanoprisms (Au TNPs) were used as substrate material of the immunosensor. The Au TNPs with two large planes were tightly modified on the electrode surface, which increased the effective contact areas with the surface of electrode compared to Au NPs (Lou et al., 2017). Thus, Au TNPs accelerated electron transfer and increased the immobilizing amount of Ab_1 effectively. With these advantages, Au TNPs as substrate material provided a stable environment for the immunosensor and improved the sensitivity of CEA detection.

In this work, the sandwich-type immunosensor was successfully designed by using the Au TNPs as the substrate material and MoS_2 NFs/Au@AgPt YNCs as labels of Ab_2. Simultaneously, the signal amplification mechanism of immunosensor was studied by using 3,3,5,5-Tetramethylbenzidine (TMB) as active substrate. And with the interaction of Au TNPs and MoS_2 NFs/Au@AgPt YNCs, the immunosensor has exhibited high sensitivity, selectivity and acceptable stability, indicating that the immunosensor has broad application prospect in clinical determination of CEA.

2. Experimental section

All the reagent and apparatus were listed in the Supporting materials.

2.1. Preparation of Au TNPs

The reported seed-growth method was adopted to synthesize pure Au TNPs (Lou et al., 2016; Scarabelli et al., 2014). The detailed process of the experimental steps was shown the Supporting materials.

2.2. Preparation of Au@AgPt YNCs

The Au@AgPt YNCs were synthesized by galvanic replacement according to a seed-growth method (Londono-Calderon et al., 2017; Londonocalderon et al., 2016). Firstly, $HAuCl_4$ (10 μL, 25 mM) solution was added to CTAC (10 mL, 75 mM) aqueous solution. After stirring for 5 min, freshly prepared $NaBH_4$ (0.6 mL, 10 mM) was injected into the above solution to obtain Au nuclei solution. Then, $HAuCl_4$ (100 μL, 20 mM) solution was dropwise added into CTAC (25 mL, 200 mM) solution, followed by the addition of AA (2.0 mL, 80 mM) solution. While the solution become transparent solution, 30 μL of Au nuclei solution was added into the above solution with continuous agitation. After remaining undisturbed for 8 h, the $AgNO_3$ (0.50 mL, 10 mM) and AA (2.0 mL, 100 mM) solution was add to the solution, respectively. Afterwards, the prepared solution was kept undisturbed at 50 °C for 8 h to obtain core-shell Au@Ag nanocubes (Au@Ag NCs). Then, 8 mL of Au@Ag NCs hydrosol solution was dispersed in flask and heated up 120 °C for 20 min with constant strong stirring. Then, 200 μL of H_2PtCl_6 (5.0 mM) solution was slowly added dropwise to the above solution under constant agitation. After 15 min of reaction, the solution was cooled to room temperature. Finally, the prepared Au@AgPt YNCs were collected by centrifugation, and then lyophilized for further use.

2.3. Preparation of MoS_2 NFs

MoS_2 NFs were synthesized using the improved method (Zhuo et al., 2013). Firstly, Mo_3O_{10}-EDA were prepared to use as precursor for synthesis of MoS_2 NFs according to the published literature (Gao et al., 2012).

Then, 0.10 g of the MoO_3-EDA was added into 20 mL of Milli-Q water and dissolved ultrasonically for 5 min, and 0.28 g of L-cysteine was dissolved to the solution under continuous stirring. The mixture was heated up 200 °C for 14 h in Teflon-lined autoclave. Finally, the MoS_2 NFs were centrifuged and washed several times with Milli-Q water, and then dried for further use.

2.4. Preparation of MoS_2 NFs/Au@AgPt YNCs

For the synthesis of MoS_2 NFs/Au@AgPt YNCs, the amino-functionalized MoS_2 NFs (NH_2–MoS_2 NFs) were prepared. In the typical procedure, 4.0 mL of MoS_2 NFs (2.0 mg mL^{-1}) was dispersed in 10 ml of anhydrous ethanol under ultrasonic condition for 15 min to get symmetrical dispersion. After that, 100 μL of APTES solution was added into above dispersion, and then heated up 100 °C for 2 h under continuous stirring. Finally, the NH_2–MoS_2 NFs were obtained by centrifugation and washing with Milli-Q water for several times.

The 4.0 mL of Au@AgPt YNCs was mixed with the prepared NH_2–MoS_2 NFs (2 mL, 2.0 mg mL^{-1}) under ultrasonic condition for 1 h to gain homogeneous dispersion. After that, the dispersion was oscillated at room temperature for 8 h to obtain the dispersion of MoS_2 NFs/Au@AgPt YNCs. The prepared MoS_2 NFs/Au@AgPt YNCs were centrifuged by washing two times with Milli-Q water, and lyophilized and collected in order to further use.

2.5. Preparation of MoS_2 NFs/Au@AgPt YNCs-Ab_2

The 4.0 mL of Ab_2 solution (20 μg mL^{-1}) was added into 4.0 mL of MoS_2 NFs/Au@AgPt YNCs dispersion (2.0 mg mL^{-1}). After shaking at 4 °C for 12 h, MoS_2 NFs/Au@AgPt YNCs-Ab_2 were obtained by centrifugation and washing with PBS (pH 7.38). After that, the precipitation was re-dissolved to 4 mL of the mixture by the addition of PBS (pH 7.38) and kept at 4 °C when not in use.

2.6. Fabrication of the immunosensor

Fig. 1 represented fabrication procedure of the sandwich-type electrochemical immunosensor. First of all, glassy carbon electrodes (GCE) were polished by alumina powder and ultrasonically washed with Milli-Q water to obtain specular surface. After that, Au TNPs (6.0 μL, 2.5 mg mL^{-1}) was modified on the prepared GCE and dried in air. Next, Ab_1 (6.0 μL, 10 μg mL^{-1}) was incubated onto the modified GCE at 4 °C for 1 h. After that, BSA (3.0 μL, 1 wt%) was immobilized onto the electrode for 1 h to block the nonspecific binding sites. Subsequently, PBS (pH 7.38) was used to thoroughly rinse the electrode to eliminate the remaining BSA. Afterwards, a series of different

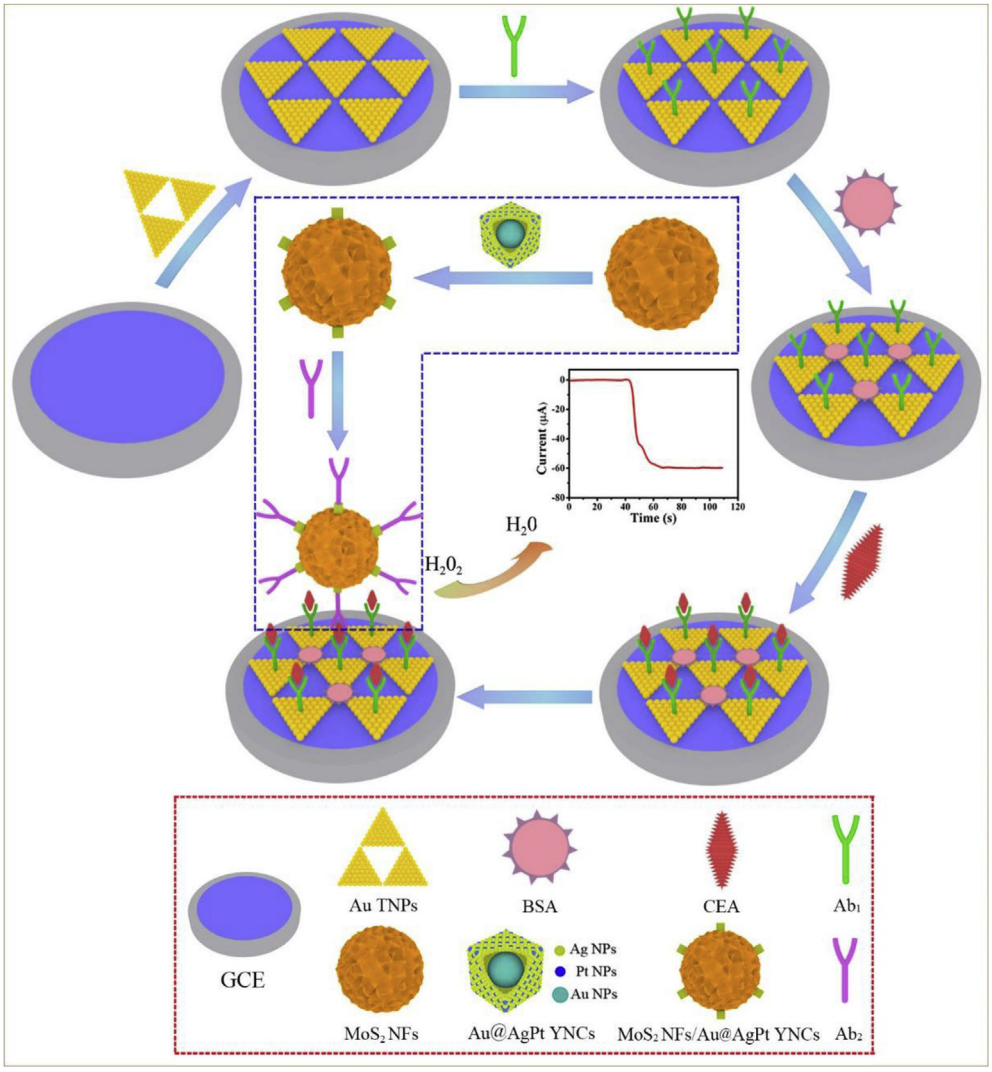

Fig. 1. Schematic representation of the preparation process of the sandwich-type electrochemical immunosensor.

concentrations of CEA were incubated on the proposed electrode at 4 °C for 1 h to ensure the specific combination between Ab_1 and CEA. Then, MoS_2 NFs/Au@AgPt YNCs-Ab_2 (6.0 μL, 2.0 mg mL^{-1}) was added dropwise to the above electrode at 4 °C for another 1 h. After that, the electrode was washed with PBS (pH 7.38) to remove any unbound Ab_2. At last, all working electrodes were kept at 4 °C for further detection.

2.7. Detection of the CEA

The amperometric measurement (i-t) was applied to measure the current response signals of the immunosensor. And PBS with 7.38 of pH was selected as electrolyte for the following electrochemical measurements. When the current kept stable, H_2O_2 (10 μL, 5.0 M) as electroactive substance was injected into the PBS (pH 7.38, 10 mL) with gentle agitation. After that, the change of current response signal was monitored by i-t curve.

3. Results and discussion

3.1. Characterization of the Au TNPs, the Au@AgPt YNCs, the MoS_2 NFs, and the MoS_2 NFs/Au@AgPt YNCs

Fig. 2A showed the TEM image of Au TNPs, it was observed that Au TNPs had average length of 140 nm and uniform morphology. The inset picture of Fig. 2A (Fig. 2a) showed a more figurative TEM image of a single Au TNPs with the edge length of about 142 nm. Fig. 2B presented HR-TEM image of Au TNPs, which displayed that the Au TNPs had the same crystallographic and stable structure.

Fig. 2C and Fig. S1C showed the TEM and SEM images of Au@AgPt YNCs, respectively. It could be found that Au@AgPt YNCs had a relatively uniform morphology with an average size about 50 nm, and the Au core remains stationary at the center of the Au@AgPt YNCs. The internal space between the AgPt alloy shell and Au core could be seen from the contrast of the HR-TEM image of Au@AgPt YNCs (Fig. 2D). Simultaneously, their elemental mapping (Fig. S2) clearly indicated that Au element was mainly distributed in the center of Au@AgPt YNCs and AgPt alloy was scattered on the exterior of Au@AgPt YNCs. The unique structure of Au@AgPt YNCs was synthesized by galvanic replacement. As shown in Fig. S1A, Au@Ag NCs (Fig. S1B) were served as the template material for the deposition of external Pt nanoparticles. In presence of Pt ions, the galvanic replacement mechanisms of Ag and Pt are already known (Jeena and Selvaraju, 2016), this is attributed that the high difference in reduction potentials between Pt (E^0 = + 1.44 V for Pt^{4+}) and Ag (E^0 = + 0.8 V for Ag^+). Fig. 2E showed the TEM image of MoS_2 NFs, the TEM image demonstrated that MoS_2 NFs had the well-stacked layered structure, which was mainly composed of MoS_2 nanosheets. Fig. 2F and G displayed the TEM and HR-TEM images of MoS_2 NFs/Au@AgPt YNCs, severally. As shown in Fig. 2F, Au@AgPt YNCs had been loaded on the surface of the MoS_2 NFs successfully. Otherwise, the EDX (Fig. S3) and the HR-TEM images of MoS_2 NFs/

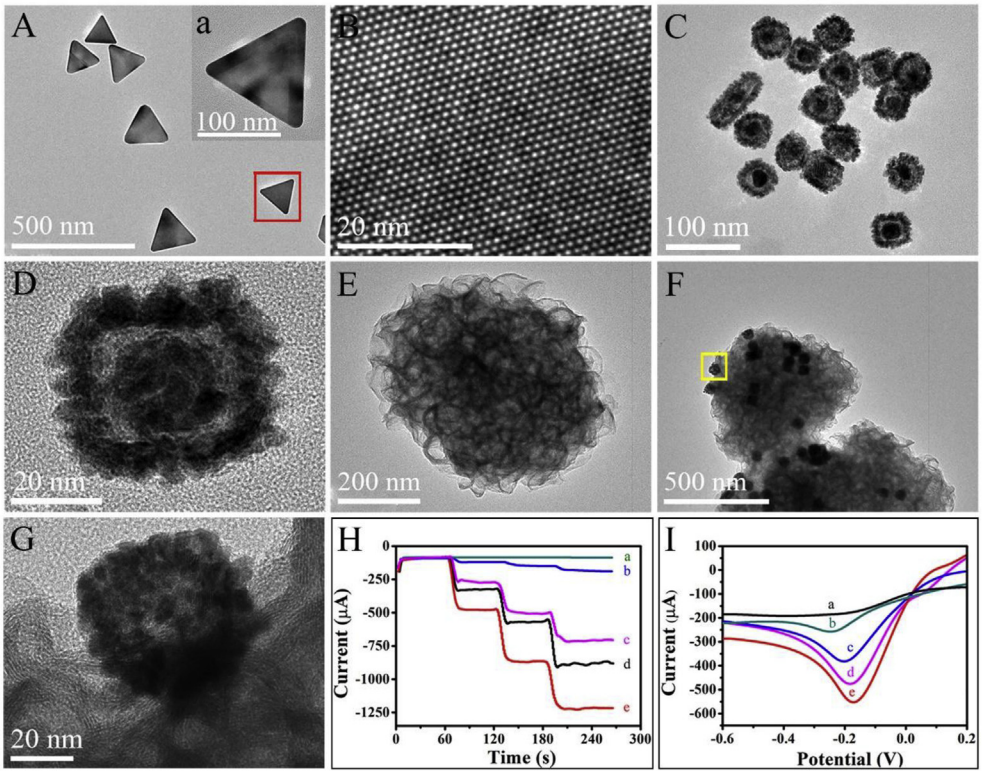

Fig. 2. (A) The TEM image of Au TNPs and a close view of the red square is shown in (a); (B) The HR-TEM image of a Au TNPs in (a); (C) The TEM image of Au@AgPt YNCs and HR-TEM image of a Au@AgPt YNCs (D); The TEM images of MoS_2 NFs (E), MoS_2 NFs/Au@AgPt YNCs (F), and (G) the HR-TEM image of the area marked with a yellow square in (F); (H) Ameperometic responses of the different modified electrodes after injecting H_2O_2 (10 μL, 5.0 M) in PBS (pH 7.38, 10 mL), and (I) the LSV response s of different modified electrodes in PBS (pH 7.38) containing 5.0 mM H_2O_2: (a) bare GCE, (b) Au TNPs, (c) MoS_2 NFs, (d) Au@AgPt YNCs, (e) MoS_2 NFs/Au@AgPt YNCs. (For interpretation of the references to color in this figure legend, the reader is referred to the Web version of this article.)

Au@AgPt YNCs further indicated that the Au@AgPt YNCs were well-adsorbed on the MoS_2 NFs.

3.2. Electrochemical characterization of the immunosensor using MoS_2 NFs/Au@AgPt YNCs as labels

The catalytic activity of the prepared nanomaterials has become a crucial factor to improve the detection sensitivity of sandwich-type immunosensor. Herein, MoS_2 NFs/Au@AgPt YNCs exhibited excellent catalytic performance for the reduction of H_2O_2. The amperometric measurement (i-t) and linear sweep voltammetry (LSV) were used to compare electrochemical response signal of different nanomaterials. The Au TNPs, Au@AgPt YNCs, MoS_2 NFs and MoS_2 NFs/Au@AgPt YNCs at the same amount (6.0 μL, 2.0 mg mL^{-1}) were modified onto bare GCE, respectively. Fig. 2H presented a typical set of i-t curves, when the current was stable, and the H_2O_2 (10 μL, 5.0 M) was injected in PBS (pH 7.38, 10 mL) to obtain current response signals of the different modified electrodes. As sketched in Fig. 2H, the bare GCE did not show the obvious current response signal (curve a), indicating that the bare GCE had no catalytic ability for the reduction of H_2O_2. When Au TNPs were coated on the bare GCE (curve b), the current signal increased slightly, this was mainly due to the good conductivity of Au TNPs. There was obvious increase of current response signal when MoS_2 NFs and Au@AgPt YNCs were modified onto the bare GCE (curve c and curve d) respectively, which indicated that MoS_2 NFs and Au@AgPt YNCs had good catalytic activity for the reduction of H_2O_2. However, when MoS_2 NFs/Au@AgPt YNCs were modified onto the bare GCE (curve e), the current response signal was further increased, which was ascribed to the synergistic effect existing in MoS_2 NFs/Au@AgPt YNCs that enhanced catalytic activity for the reduction of H_2O_2.

In order to further demonstrate the catalytic performances of MoS_2 NFs/Au@AgPt YNCs, the LSV was used to record current response signal of the modified electrode. Fig. 2I displayed a typical set of LSV curves recorded between - 0.6 V and +0.2 V in 10 mL PBS (pH 7.38) with 5.0 mM H_2O_2. Similarly, when Au TNPs, MoS_2 NFs, Au@AgPt YNCs and MoS_2 NFs/Au@AgPt YNCs were loaded on bare GCE respectively, evident differences could be seen for every electrode with respect to the peak shape, the reductive peak potential, and the magnitude of the reduction current. Among them, MoS_2 NFs/Au@AgPt YNCs still produced the largest reductive peak current (curve e), indicating that MoS_2 NFs/Au@AgPt YNCs had the most active catalytic effect on the reduction of H_2O_2. These results revealed that MoS_2 NFs/Au@AgPt YNCs could be used as the labels of Ab_2 to amplify the current response signal.

3.3. The signal amplification mechanism of the immunosensor

In order to study the amplification of current signal in the immunosensor, the MoS_2 NFs, Au@AgPt YNCs and MoS_2 NFs/Au@AgPt YNCs were used as the labels of Ab_2 to fabricate the immunosensor, respectively. As shown in Fig. 3A, when MoS_2 NFs-Ab_2 (curve b), Au@AgPt YNCs-Ab_2 (curve c) and MoS_2 NFs/Au@AgPt YNCs-Ab_2 (curve d) were incubated onto the electrode (CEA/BSA/Ab_1/Au TNPs/GCE, curve a) respectively, curve b exhibited a very small current signal. This was because MoS_2 NFs with weak biocompatibility were difficult to incubate Ab_2, thus it was hard to specifically bind with CEA and immobilize on the electrode surface. However, curve d showed significant current response signals, which indicated that the introduction of Au@AgPt YNCs improved the poor biocompatibility and conductivity of MoS_2 NFs. In addition, curve d showed higher current response signals than curve c. The result indicated MoS_2 NFs/Au@AgPt YNCs as labels of Ab_2 could amplify the current signal more effectively compared with Au@AgPt YNCs, which was ascribed to synergistic effect of Au@AgPt YNCs and MoS_2 NFs. Therefore, MoS_2 NFs/Au@AgPt YNCs were used as the labels of Ab_2 to amplify current signal and improve the sensitivity in the detection of CEA.

The signal amplification of the immunosensor was mainly achieved by MoS_2 NFs/Au@AgPt YNCs catalyzing the reduction of H_2O_2. In order to study the catalytic mechanism of MoS_2 NFs/Au@AgPt YNCs, TMB was used as active substrate to monitor the existence of hydroxyl radicals (OH_{ad}) according to changes of its color (Jiao et al., 2017; Liu et al., 2012b). As shown in Fig. 3B, the electrodes modified with MoS_2

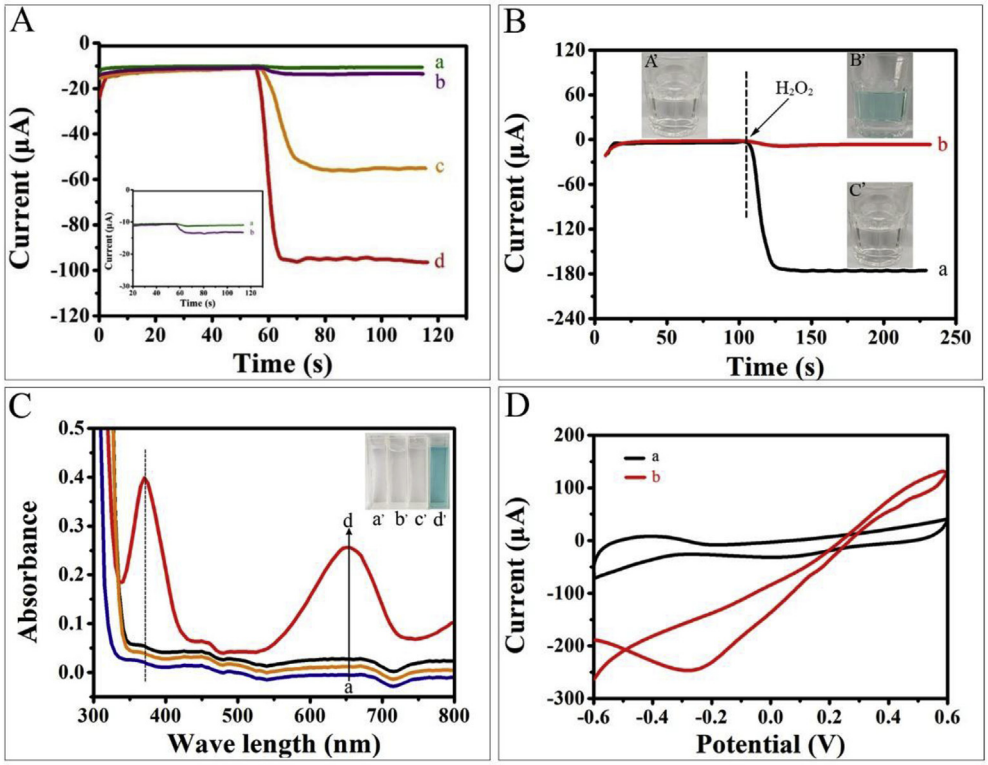

Fig. 3. (A) Ameperometic responses of the different modified electrodes after injecting H_2O_2 (10 μL, 5.0 M) in PBS (pH 7.38): (a) CEA/BSA/Ab_1/Au TNPs/GCE, (CEA: 1.0 ng mL^{-1}); (b) MoS_2 NFs-Ab_2/CEA/BSA/Ab_1/Au TNPs/GCE.; (c) Au@AgPt YNCs-Ab_2/CEA/BSA/Ab_1/Au TNPs/GCE; (d) MoS_2 NFs/Au@AgPt YNCs-Ab_2/CEA/BSA/Ab_1/Au TNPs/GCE; (B) The i-t curve of the absence of TMB (a) and the presence of TMB (5 mM) (b) in PBS, the color photographs of solution: before injecting H_2O_2 (A); after injecting H_2O_2 (5 μL, 5.0 M) in b (B) and in a (C); (C) The UV–vis spectras of MoS_2 NFs/Au@AgPt YNCs and TMB (a), H_2O_2 and TMB (b), TMB (c), TMB and H_2O_2 and MoS_2 NFs/Au@AgPt YNCs (d), the internal photographs of the reactions correspond from left to right; (D) The CV with (a) absence of H_2O_2 and (b) presence of H_2O_2 (2.5 mM) in PBS. (For interpretation of the references to color in this figure legend, the reader is referred to the Web version of this article.)

NFs/Au@AgPt YNCs were carried out by i-t curve for the absence of TMB (a) and the presence of TMB (b), respectively. Before injecting H_2O_2, the colors of substrate were colorless in internal photograph (A). When H_2O_2 was injected in a and b respectively, curve a showed obvious current response signal, and the color of substrate was still colorless in internal photograph (C). However, curve b showed very small current response and the color of substrate began to be blue in internal photograph (B). The result indicated that the process of catalyzing H_2O_2 might produce OH_{ad}, and OH_{ad} rapidly oxidized TMB to the blue oxidation product, thus curve a produced very small current response. Simultaneously, UV–visible spectroscopy was used to further measure the blue product. As shown in Fig. 3C, when H_2O_2 (curve a) and MoS_2 NFs/Au@AgPt YNCs (curve b) were added in TMB solution respectively, the absorption peaks could not be seen and their colors were colorless in the internal photographs (a' and b). After adding MoS_2 NFs/Au@AgPt YNCs to the TMB solution containing H_2O_2, the mixture changed from colorless to blue and exhibited two strong absorption peaks centered at 371 nm and 653 nm (curve d), which was typically attributed to the oxidation of TMB by OH_{ad} (Josephy et al., 1982; Yujun et al., 2010). Moreover, the electrodes were further measured by cyclic voltammetry scan (CV) from −0.6 V to 0.6 V with absence of H_2O_2 (curve a) and presence of H_2O_2 (curve b) in Fig. 3D, respectively. Only the obvious reduction peak could be obtained in presence of H_2O_2, which indicated that the process of MoS_2 NFs/Au@AgPt catalyzing H_2O_2 was a reduction reaction. Therefore, according to the literature (Venrooij and Koper, 1995), the signal amplification mechanism of immunosensor could be summarized as follows:

$$H_2O_2 + e^- \xrightarrow{MoS_2\ NFs/Au@AgPt} OH_{ad} + OH^- \quad (1)$$

$$OH_{ad} + e^- \rightarrow OH^- \quad (2)$$

$$2OH^- + 2H^+ \rightarrow 2H_2O \quad (3)$$

In addition, the reaction 2 would be terminate in the presence of TMB, and OH_{ad} rapidly oxidized TMB (colorless) to be oxidized TMB (blue) (Dutta et al., 2013) thus curve b showed smaller current response compared with curve a in Fig. 3B. Therefore, the MoS_2 NFs/Au@AgPt YNCs with excellent catalytic activity could effectually catalyze the reduction of H_2O_2 and achieve signal amplification of the immunosensor.

3.4. Characterization of the immunosensor

The immobilizing amount of Ab_2 on the prepared nanocomposites is a key factor for the determination of CEA in the immunosensor. Herein, UV–visible spectroscopy was applied to estimate the immobilizing amount of Ab_2 on MoS_2 NFs/Au@AgPt YNCs. As shown in Fig. 4A, the peak at 279 nm was a typical absorption of protein, and the absorbance increased continuously with the increase of Ab_2 concentration. The absorbance and the concentration of Ab_2 showed a linear relationship in the insert of Fig. 4A. And the standard curve was A = 0.00676 C + 0.0578, where A was the absorbance of Ab_2 solution at 279 nm, C (μg mL^{-1}) was the concentration of Ab_2 solution, and the correlation coefficient was 0.996. Therefore, the immobilizing amount of Ab_2 on MoS_2 NFs/Au@AgPt YNCs was calculated by the above standard curve after conjugation. The absorbance of supernatant was measured five times by UV–visible spectroscopy at same conditions, and the detailed data was shown in Table S1. The result indicated that the average immobilizing amount of Ab_2 on 1.0 mg of MoS_2 NFs/Au@AgPt YNCs was 5.71 μg, which was enough for the designed immunosensor. In addition, curve b and c represented the immunosensor using Au nanoparticle (Au NPs) and Au TNPs as substrate material in Fig. 4B, respectively. As expected, Au TNPs as substrate material could exhibit better electrochemical performances, which might because Au TNPs had the larger contact area with the electrode surface.

Electrochemical impedance spectra (EIS) has become an effective and convenient measurement to monitor the interface electrochemical characteristics of the modified electrode. The semicircular diameter at high frequencies is associated with the electron transfer resistance (R_{et}), and at low frequencies the linear portion corresponds to the diffusion process in the impedance spectra (Wu et al., 2015). Herein, a comparative study of EIS was applied to characterize the step-by-step assembly process of immunosensors. As shown in Fig. 4C, the bare GCE

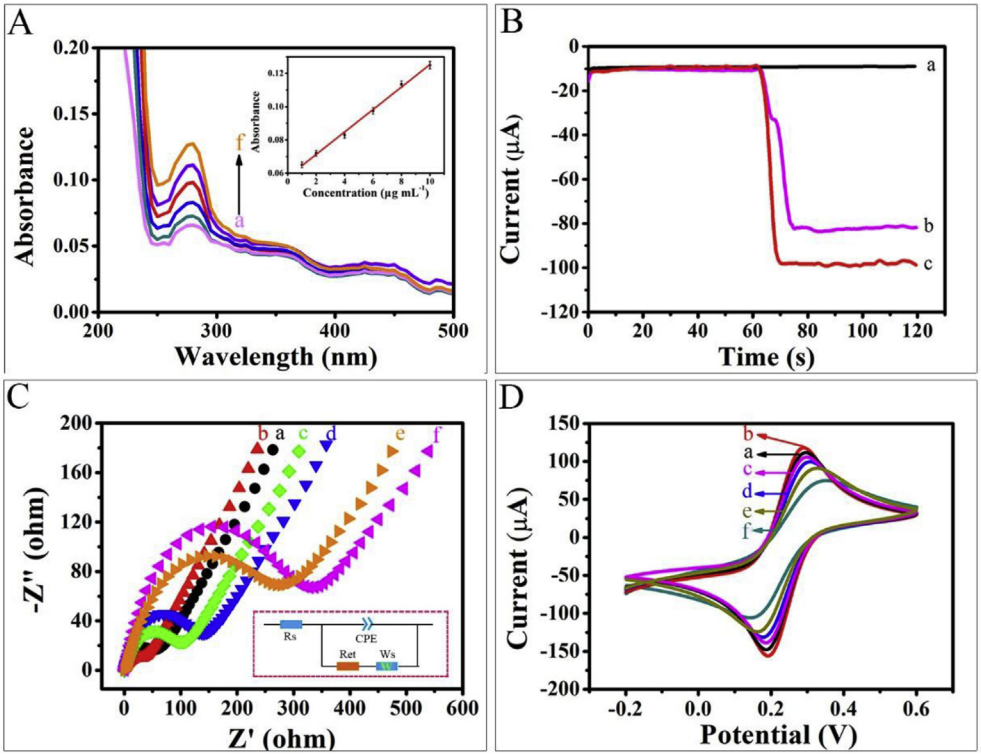

Fig. 4. (A) UV–vis spectra for different concentration of Ab_2 solution, from a to f: 1.0 μg mL^{-1}, 2.0 μg mL^{-1}, 4.0 μg mL^{-1}, 6.0 μg mL^{-1}; (e) 8.0 μg mL^{-1}; (f) 10.0 μg mL^{-1}, the insert of panel A is the standard curve of Ab_2 solution in 279 nm; (B) Amperometric i-t curves of the immunosensor for the detection of 1.0 ng mL^{-1} CEA: (a) GCE; (b) MoS_2 NFs/Au@AgPt YNCs-Ab_2/CEA/BSA/Ab_1/Au TNPs/GCE; (c) MoS_2 NFs/Au@AgPt NCs-Ab_2/CEA/BSA/Ab_1/Au TNPs/GCE; (C) EIS recorded from 0.5 to 10^5 Hz in PBS (pH 7.38) containing 0.1 M KCl and 2.5 mM Fe$(CN)_6^{3-}$/Fe$(CN)_6^{4-}$ and (D) CV scanned from - 0.2 V to 0.6 V in 5.0 mM $K_3Fe(CN)_6$ containing 0.1 M KCl with a scan rate of 100 mV/s obtained for each immobilized step: (a) GCE, (b) Au TNPs/GCE, (c) Ab_1/Au TNPs/GCE, (d) BSA/Ab_1/Au TNPs/GCE, (e) CEA/BSA/Ab_1/Au TNPs/GCE, and (f) MoS_2 NFs/Au@AgPt YNCs-Ab_2/CEA/BSA/Ab_1/Au TNPs/GCE.

displayed a very small semicircle domain (curve a) at high frequencies. When the Au TNPs were modified onto the electrode, the semicircle diameter significantly lowered (curve b), demonstrating that Au TNPs as superior conductive nanomaterials could accelerate the interface electron transfer. However, when Ab_1 (curve c), BSA (curve d), CEA (curve e) and the MoS_2 NFs/Au@AgPt YNCs-Ab_2 (curve f) were layer by layer modified onto the electrode, the semicircle diameter increased gradually. This was because the protein films hindered the transfer of interface electrons. During the modification processes of electrodes, the value of R_{et} is suitable to study the interfacial electrochemical properties of the modified electrodes. And as shown in Table S2, the corresponding values of R_{et} were obtain by fitting with ZSimpwin software. These results indicated that the layer-by-layer assembly process of immunosensor was successful.

The CV was employed to further characterize the modified electrodes. As shown in Fig. 4D, the modified electrodes were measured by CV from - 0.2–0.6 V in 5.0 mM $K_3[Fe(CN)_6]$ solution containing 0.1 M KCl with the scan rate of 100 mV/s. It could be seen that the bare GCE (curve a) showed a pair of definite reduction/oxidation peaks. When the Au TNPs were coated onto the electrode (curve b), the redox peak current was significantly higher compare with bare GCE. After that, when Ab_1 (curve c), BSA (curve d), CEA (curve e) and MoS_2 NFs/Au@AgPt YNCs-Ab_2 (curve f) were sequentially incubated to the modified electrode, the redox peak current began to decrease gradually. These results were consistent with the changes observed by EIS in Fig. 4 C, which also demonstrated the successful fabrication of the immunosensor.

3.5. Optimization of the experimental conditions

In order to be more sensitive to detecte the CEA, the conditions of the experiment including the pH of PBS, the concentrations of Au TNPs and MoS_2 NFs/Au@AgPt YNCs were optimizated. In this experiment, the immunosensors were fabricated with the same concentration CEA (1.0 ng mL^{-1}). And i-t curve was used to monitor the change of current signal in different experimental conditions after injecting H_2O_2 (10 μL, 5.0 M) into PBS (10 mL).

The proper pH of PBS plays an important factor in the performance of immunosensor, this is because the strong acid or alkaline electrolyte may disrupt the activity of biological molecules and affects the sensitivity of immunosensor. A series of pH were tested to study the performance of the immunosensor to obtain the proper pH of PBS. As displayed in Fig. 5A, when the pH changed from 5.84 to 7.38, the current signal of the immunosensor gradually increased. When the pH further increased, the current signal began to decrease. Simultaneously, the CV was employed to further study the pH effect on the response of biosensor. As shown in Fig. 5B, cathodic potential shifted negatively with the increase of pH. The reductive peak current increased with increasing pH values from 5.84 to 7.38, and then decreased when the pH was over 7.38. The result indicated that the pH of 7.38 could keep the best biological activity for biological molecules and exhibit optimal current response signals. Therefor, PBS with pH of 7.38 was used as the electrolyte of the immunosensor for the whole studies.

The concentration of Au TNPs also plays a key role in the interface electron transfer and the immobilizing of Ab_1. Fig. 5C showed the optimization results of Au TNPs, it was found that the current signal raised gradually as the concentration of Au TNPs increased. However, when the concentration of Au TNPs increased to 2.5 mg mL^{-1}, its signal reached maximum value. After that, the current signal continued to decrease, thus 2.5 mg mL^{-1} of Au TNPs was chosen as the optimal concentration.

Furthermore, the amount of MoS_2 NFs/Au@AgPt YNCs is another important factor that affects its electrochemical performances. Thus, in order to obtain the optimal concentration of MoS_2 NFs/Au@AgPt YNCs. The concentration of MoS_2 NFs/Au@AgPt YNCs was optimizated in Fig. 5D, it was observed that as the concentration of MoS_2 NFs/Au@AgPt YNCs increased from 0.5 to 2.0 mg mL^{-1}, the current signal significantly increased. However, when the concentration of MoS_2 NFs/Au@AgPt YNCs was further increased, the current signal began to decrease gradually. It was inferred that 2 mg mL^{-1} of MoS_2 NFs/Au@AgPt YNCs could improve the ability to catalyze H_2O_2 and amplify current signal of the immunosensor. Hence, 2.0 mg mL^{-1} of MoS_2 NFs/Au@AgPt YNCs was selected as the optimal concentration.

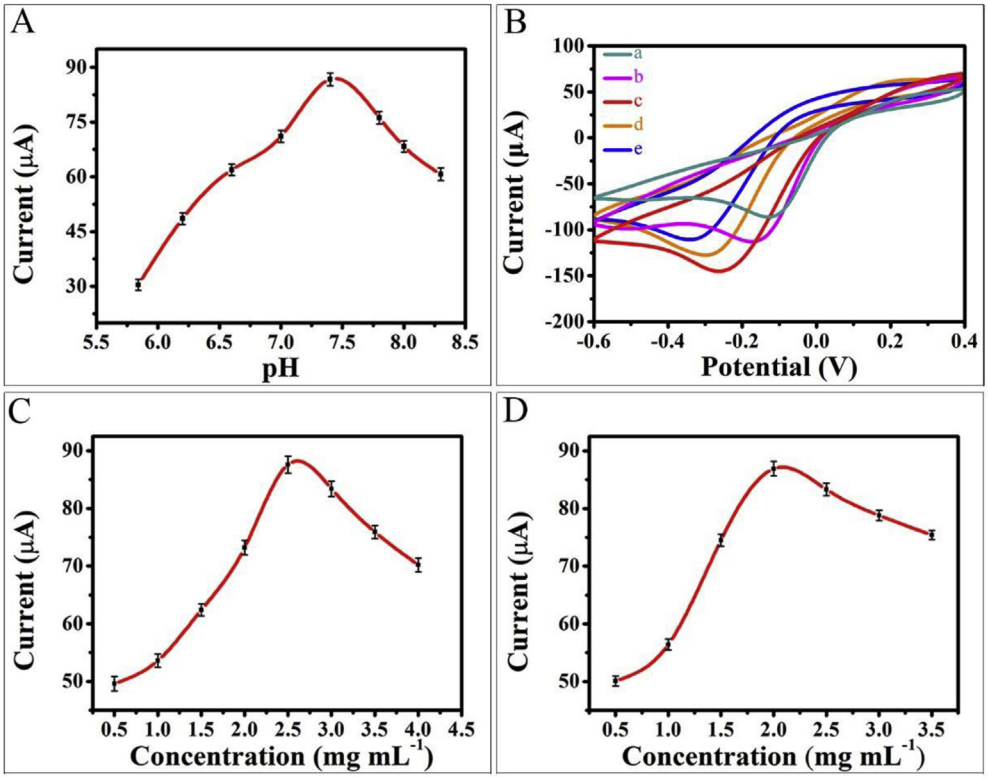

Fig. 5. Effect of pH (A), the concentrations of Au TNPs (C), MoS_2 NFs/Au@AgPt YNCs (D) on the current change of the immunosensor during the detection of 1.0 ng mL^{-1} CEA in PBS after injecting H_2O_2 (10 μL, 5.0 M); (B) CV of the immunosensor in PBS containing 5 mM H_2O_2 at different pH: (a) 5.84, (b) 6.64, (c) 7.38, (d) 7.73, (e) 8.34.

3.6. Analytical performance of the immunosensor

Under the optimal experimental conditions, the sandwich-type electrochemical immunosensor using Au TNPs as substrate material and MoS_2 NFs/Au@AgPt YNCs-Ab_2 as signal amplifier was applied to detect quantitatively a series of different concentrations of CEA by i-t curve in PBS. As displayed in Fig. 6A, the currrent signal raised gradually as the concentration of CEA increased from 10 fg mL^{-1} to 100 ng mL^{-1}. As shown in Fig. 6B, the calibration curve exhibited a good linear relationship between the current signal and logarithm of the CEA concentration, and the regression equation of the calibration curve was $I = 13.23 \lg c + 84.07$ with correlation coefficient of 0.9982. The detection limit (LOD) of the immunonsensor was determined to be 3.09 fg mL^{-1} (calculation details see Supporting materials). The proposed immunonsensor had the characteristics of high sensitivity, a low detection limit and broad detection range compared with the analytical performances of previous immunosensors (Table S3). These results demonstrated that the fabricated immunosensor provided a effective method for high sensitivity determination of CEA. The sandwich-type electrochemical immunosensor exhibited excellent performances, this might be related to the following aspects: (1) owing to the high contact areas with the surface of electrode and excellent conductivity of Au TNPs, which could increase significantly the immobilizing amount of Ab_1 and accelerate electron transfer; (2) MoS_2 NFs/Au@AgPt YNCs had benign biocompatibility and excellent catalytic activity towards the reduction of H_2O_2 because of the synergistic effect presenting in MoS_2 NFs/Au@AgPt YNCs.

3.7. Reproducibility, selectivity, and stability of the immunosensor

In order to study reproducibility of the immunosensor, the five immunosensors were fabricated and detected at the same concentration of CEA (1 ng mL^{-1}) in Fig. S4A. The relative standard deviation (RSD) of the measurements for the five immunosensors was 2.36%, which meant that the immunosensor had acceptable reproducibility. To investigate selectivity of the immunosensor, the CEA solution that contained 100 ng mL^{-1} of interfering substances (PSA, HBs, BSA, and AFP) was incubated and measured, respectively. As dispalyed in Fig. S4B, the immunosensors with the CEA exhibited obviously higher current signal than those without the CEA. The change of current signal caused by the

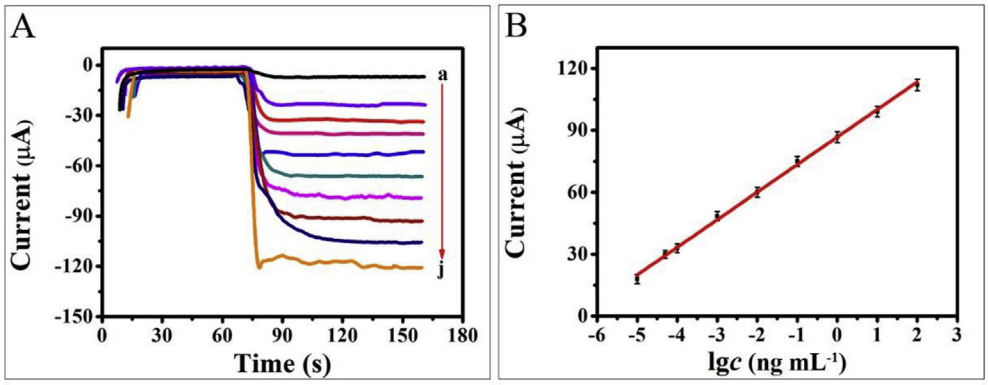

Fig. 6. (A) Amperometric response of the immunosensor for the detection of different concentrations of CEA, from a to j: 0 ng mL^{-1}, 10 fg mL^{-1}, 50 fg mL^{-1}, 100 fg mL^{-1}, 1.0 pg mL^{-1}, 10 pg mL^{-1}, 100 pg mL^{-1}, 1.0 ng mL^{-1}, 10 ng mL^{-1}, 100 ng mL^{-1}; (B) Calibration curve of the immunosensor for the detection of different concentrations of CEA, error bar = SE (n = 5).

interfering substances was less than 5% compared with non-interferences, which indicated the fabricated immunosensor had good selectivity. In addition, the stability of the immunosensor was also studied by storing the immunosensor at 4 °C, and detected every 5 days. The result was shown in Fig. S4C, it was observed that the current signal of the immunosensor decreased to 87.5% of its initial response after 25 days. The results indicated the designed immunosensor had satisfactory stability, this might be attributed to the good stability of Au TNPs and benign biocompatibility of MoS_2 NFs/Au@AgPt YNCs.

3.8. Real sample analysis

In order to verify the reliability and accuracy of the proposed immunosensor, the different concentrations of CEA in human serum were used to study its recoveries by standard addition methods. The human serum samples were provided from the school infirmary. And the samples 1–4 (990 μL) were prepared by adding 10.0 μL of CEA (100 ng mL^{-1}, 500 ng mL^{-1}, 1000 ng mL^{-1}, respectively) and analyzed by the immunosensor via i-t. The result was displayed in Table S4, the RSD ranged from 2.969% to 1.156% and the recovery rate was from 99.8% to 101.0%, indicating that the immunosensor has a promising approach for quantitative detection of CEA in serum samples.

4. Conclusion

In short, a sensitive sandwich-type electrochemical immunosensor was fabricated successfully by using Au TNPs as the substrate material and utilizing MoS_2 NFs/Au@AgPt YNCs as labels of Ab_2 to quantitatively detect CEA. With the favorable cooperation of Au TNPs and MoS_2 NFs/Au@AgPt YNCs, the immunosensor showed broad detection range (10 fg mL^{-1} to 100 ng mL^{-1}), a low detection limit (3.09 fg mL^{-1}), good selectivity and reproducibility. Although the satisfactory results were obtained, there is still a challenge for us to simplify the fabrication procedure of immunosensor to meet the needs of clinical examination, which is the direction for further research.

CRediT authorship contribution statement

Enhui Ma: Conceptualization, Methodology, Software, Data curation, Writing - original draft. **Ping Wang:** Visualization, Investigation, Validation. **Qingshan Yang:** Software, Validation. **Haoxuan Yu:** Software, Validation. **Fubin Pei:** Software, Validation. **Yueyun Li:** Supervision, Investigation. **Qing Liu:** Supervision, Investigation. **Yunhui Dong:** Resources, Supervision.

Acknowledgments

This study was financially supported by the Natural Science Foundation of China (No. 21575079) and the Key Research and Development Program of Shandong Province (No.2018GSF120001). All of the authors express their deep thanks.

Appendix A. Supplementary data

Supplementary data to this article can be found online at https://doi.org/10.1016/j.bios.2019.111580.

References

Baghayeri, M., Amiri, A., Alizadeh, Z., Veisi, H., Hasheminejad, E., 2018a. J. Electroanal. Chem. 810, 69–77.
Baghayeri, M., Ansari, R., Nodehi, M., Razavipanah, I., Veisi, H., 2018b. Microchimica Acta 185, 320.
Baghayeri, M., Veisi, H., 2015. Biosens. Bioelectron. 74, 190–198.
Baghayeri, M., Zare, E.N., Lakouraj, M.M., 2014. Biosens. Bioelectron. 55, 259–265.
Choi, S.H., Hong, Y.J., Kang, Y.C., 2013. Nanoscale 5, 7867–7871.
Dutta, A.K., Das, S., Samanta, S., Samanta, P.K., Adhikary, B., Biswas, P., 2013. Talanta 107, 361–367.
Dixit, C.K., Vashist, S.K., O'Neill, F.T., O'Reilly, B., Maccraith, B.D., O'Kennedy, R., 2010. Anal. Chem. 82, 7049–7052.
Gao, Q., Wang, S., Fang, H., Weng, J., Zhang, Y., Mao, J., Tang, Y., 2012. J. Mater. Chem. 22, 4709–4715.
Guo, Y., Xu, Y.-T., Zhao, B., Wang, T., Zhang, K., Yuen, M.M., Fu, X.-Z., Sun, R., Wong, C.-P., 2015. J. Mater. Chem. 3, 13653–13661.
Gupta, V.K., Yola, M.L., Qureshi, M.S., Solak, A.O., Atar, N., Üstündağ, Z., 2013. Sens. Actuators B Chem. 188, 1201–1211.
Hong, Y.J., Son, M.Y., Park, B.K., Kang, Y.C., 2013. Small 9, 2224–2227.
Hu, Z., Wang, L., Zhang, K., Wang, J., Cheng, F., Tao, Z., Chen, J., 2014. Angew. Chem. Int. Ed. 53, 12794–12798.
Jeena, S.E., Selvaraju, T., 2016. J. Chem. Sci. 128, 357–363.
Jiao, L., Zhang, L., Du, W., Liu, S., Wei, Q., Li, H., 2017. Electrochim. Acta 252, 374–380.
Josephy, P.D., Eling, T., Mason, R.P., 1982. J. Biol. Chem. 257, 3669–3675.
Limbut, W., Kanatharana, P., Mattiasson, B., Asawatreratanakul, P., Thavarungkul, P., 2006. Biosens. Bioelectron. 22, 233–240.
Litvak, A., Cercek, A., Segal, N., Reidylagunes, D., Stadler, Z.K., Yaeger, R.D., Kemeny, N.E., Weiser, M.R., Pessin, M.S., Saltz, L., 2014. J. Natl. Compr. Cancer Netw. 12, 907–913.
Liu, A., 2008. Biosens. Bioelectron. 24, 167–177.
Liu, J., Yang, H.Q., Kleitz, F., Chen, Z.G., Yang, T., Strounina, E., Lu, G.Q., Qiao, S.Z., 2012a. Adv. Funct. Mater. 22, 591–599.
Liu, S., Tian, J., Wang, L., Sun, X., 2012b. Sens. Actuators, B 165, 44–47.
Lohani, C.R., Neupane, L.N., Kim, J.M., Lee, K.H., 2012. Sens. Actuators, B 161, 1088–1096.
Londono-Calderon, A., Bahena, D., Yacaman, M.J., 2016. Langmuir 32, 7572–7581.
Londono-Calderon, A., Campos-Roldan, C.A., González-Huerta, R.G., Hernandez-Pichardo, M.L., Angel, P.D., Yacaman, M.J., 2017. Int. J. Hydrogen Energy 42, 30208–30215.
Londonocalderon, A., Bahena, D., Joséyacamán, M., 2016. Langmuir 32, 7572.
Lou, Z., Fujitsuka, M., Majima, T., 2016. ACS Nano 10, 6299–6305.
Lou, Z., Fujitsuka, M., Majima, T., 2017. J. Phys. Chem. Lett. 8, 844–849.
Pan, Y., Zhou, J., Su, K., Hu, N., Wang, P., 2017. Procedia Technol. 27, 214–216.
Scarabelli, L., Coronadopuchau, M., Ginercasares, J.J., Langer, J., Lizmarzán, L.M., 2014. ACS Nano 8, 5833.
Smolej, L., Benesova, P., 2010. Cancer 107, 2742–2743.
Teng, Z., Wang, S., Su, X., Chen, G., Liu, Y., Luo, Z., Luo, W., Tang, Y., Ju, H., Zhao, D., Lu, G., 2014. Adv. Mater. 26, 3741–3747.
Venge, P., Roxin, L.E., Olsson, I., 2010. Br. J. Haematol. 37, 331–335.
Venrooij, T.G.J.V., Koper, M.T.M., 1995. Electrochim. Acta 40, 1689–1696.
Wang, L., Dou, H., Lou, Z., Zhang, T., 2013. Nanoscale 5, 2686–2691.
Wu, D., Ma, H., Zhang, Y., Jia, H., Yan, T., Wei, Q., 2015. ACS Appl. Mater. Interfaces 7, 18786–18793.
Xie, J., Zhang, J., Li, S., Grote, F., Zhang, X., Zhang, H., Wang, R., Lei, Y., Pan, B., Xie, Y., 2013. J. Am. Chem. Soc. 135, 17881–17888.
Xu, R., Lu, P., Wu, B., Wang, X., Pang, X., Du, B., Fan, D., Wei, Q., 2018. Sens. Actuators B Chem. 274, 349–355.
Yola, M.L., Atar, N., 2014. Electrochim. Acta 119, 24–31.
Yola, M.L., Atar, N., Eren, T., Karimi-Maleh, H., Wang, S., 2015. RSC Adv. 5, 65953–65962.
Yola, M.L., Atar, N., Üstündağ, Z., Solak, A.O., 2013. J. Electroanal. Chem. 698, 9–16.
Yujun, S., Konggang, Q., Chao, Z., Jinsong, R., Xiaogang, Q., 2010. Adv. Mater. 22, 2206–2210.
Zhou, Y., Zhuo, Y., Liao, N., Chai, Y., Yuan, R., 2014. Chem. Commun. 50, 14627–14630.
Zhuo, S., Xu, Y., Zhao, W., Zhang, J., Prof, #x, Zhang, D.B., 2013. Angew. Chem. Int. Ed. 52, 8602–8606.